Numerical analysis of heat load distribution in Heliotron J with magnetic field tracing and plasma transport modeling

R. Matoike[1], G. Kawamura[2,3], S. Ohshima[4], Y. Suzuki[2,3], M. Kobayashi[2,3], S. Masuzaki[2], S. Kobayashi[4], S. Kado[4], T. Minami[4], H. Okada[4], T. Mizuuchi[4], S. Konoshima[4], Y. Feng[5], H. Frerichs[6], K. Nagasaki[4]

[1]Graduate School of Energy Science, Kyoto University, Uji, 611-0011, Japan
[2]National Institute for Fusion Science, National Institute of Natural Sciences, Toki, 509-5292, Japan
[3]Department of Fusion Science, Graduate University for Advanced Science, SOKENDAI, Toki, 509-5292, Japan
[4]Institute of Advanced Energy, Kyoto University, Uji, 611-0011, Japan
[5]Max-Planck-Institut fr Plasmaphysik, D-17491 Greifswald, Germany
[6]Department of Engineering Physics, University of Wisconsin - Madison, Madison, WI 53706, USA

E-mail: matoike.ryota.62c@st.kyoto-u.ac.jp

May 2021

Abstract. We model and characterize the heat load patterns on the vacuum chamber wall in an advanced helical device, Heliotron J, based on the peripheral transport code EMC3-EIRENE, in three typical magnetic configurations with different toroidal mirror ratios (bumpiness). The heat flux distribution on the vacuum chamber wall evaluated with the EMC3-EIRENE code shows several groups of heat flux footprints, some of which are not seen in the connection length distribution obtained with the magnetic field tracing code. This clearly shows the necessity for plasma modeling in addition to magnetic field line tracing in the design of three-dimensional devices. At high electron density, a displacement and an expansion of the heat flux distribution in both the toroidal and poloidal directions are observed. As a result of the heat flux expansion, the peak value of the heat flux decreases at high electron density. Further, an approach that uses the heat distribution function is proposed to evaluate the global power distribution in the entire vacuum chamber. The evaluation results confirm a decrease in the peak heat flux and an increase in the plasma-wetted area at high electron density. The heat flux distribution expansion is larger for the low-bumpiness configuration, in which the peak heat value is by more than 15% lower than that for the high-bumpiness configuration.

Keywords: divertor, modeling, heat load, connection length, Heliotron J, EMC3-EIRENE

1. Introduction

A high heat load on a plasma-facing component is a critical issue for realizing fusion devices. The engineering limit of heat load on the divertor plate is determined by the thermal conductivity of the material and the cooling performance, and hence a drastic increase of this limit is difficult to achieve. An understanding of the mechanism of heat/particle transport in the scrape-off layer (SOL) region is required for predicting the heat load on divertor plates. For tokamak divertor configurations, the shape of the footprint on the poloidal divertor has been formulated [1] and the power width λ_q has been used [2] for multi-machine comparisons. The heat and particle flux in a divertor can be controlled by modifying the divertor configuration, as done with long-leg [3, 4] and snowflake [5, 6] divertors, or by introducing a three dimensional (3D) magnetic structure with resonant magnetic perturbation (RMP) [7, 8, 9, 10].

The physics of these advanced divertors in tokamak devices is similar to that of divertor in helical devices such as stellarators and heliotrons because helical devices have an inherent 3D magnetic field topology and thus a 3D divertor structure. However, the heat and particle transport is complicated in such a 3D configuration, and a simple formulation similar to that for the divertor footprint width in tokamaks is difficult because cross-field transport is more prominent due to the introduction of three-dimensionality. In addition, the competition between cross-field and parallel transport plays an essential role in the transport and structure of divertor plasma [11].

For the design of such advanced fusion devices with complicated magnetic field geometries, an understanding of the 3D physics in divertor plasma transport is required. Numerical modeling of peripheral plasma is a powerful tool for facilitating the understanding of plasma transport against the SOL magnetic field structure. The peripheral plasma transport code EMC3-EIRENE [12, 13] has been applied to various stellarators [12, 14, 15, 16] and tokamak devices [17, 18]. This code can model the heat/particle flux distribution including the effects of parallel transport, cross-field transport and plasma-surface interaction. EMC3-EIRENE has recently been applied to Heliotron-J [19], a medium-sized helical-axis heliotron device with flexible magnetic field configurations to study SOL plasma transport in a 3D machine [20]. Heliotron J allows the magnetic configurations, including the topology of the SOL magnetic field structure, to be flexibly controlled in a single device. The characterization of the heat load distribution for various magnetic configurations would serve as a basis for understanding the heat transport induced by the magnetic field geometry and would thus benefit divertor optimization.

This work is a first attempt to characterize the heat flux distribution and its density dependence in three typical magnetic configurations of Heliotron J. The configurations have different toroidal mirror ratios (bumpiness), which control neoclassical transport. Bumpiness is a key parameter for optimization of stellarators and heliotrons. The rest of this paper is organized as follows. In section 2, we describe the peripheral magnetic structure of Heliotron J and present the difference in footprint patterns between the

connection length calculated with field line tracing code and the heat flux calculated with EMC3-EIRENE modeling. In section 3, we discuss the effects of the electron density and magnetic configurations on the heat flux distribution. The peak heat flux decreases and shifts in the poloidal and toroidal directions at high electron density. To investigate the dependence of the heat load on the plasma density and the magnetic configuration of the divertor plasma, we propose a method for evaluating the heat load profile as a statistic for the whole vacuum vessel wall. Finally, conclusions are presented in section 4.

2. Footprint structure obtained with magnetic field tracing and transport analysis

2.1. Peripheral magnetic structure obtained with magnetic field tracing code

Heliotron J is a helical-axis heliotron device with a major radius of $R = 1.2$ m and a field strength on the axis of $B_0 \leq 1.5$ T. The standard magnetic configuration of Heliotron J has an $n = 4$ toroidal periodicity and $m = 7$ poloidal mode structures, as shown in figure 1. The coil currents are controlled by five independent power supplies, giving flexibility to the magnetic configurations. In the helical heliotron concept, bumpiness [21, 22], the toroidal ripple component, is a parameters for controlling the neo-classical transport. The magnetic field strength is higher (lower) at the corner (straight) sections in the standard configuration of Heliotron J. Three configurations with different degrees of bumpiness are selected for analysis in this paper. The magnetic field strength along the toroidal direction for different degrees of bumpiness (high, medium, and low) configurations is shown in figure 2. The rotational transform and the volume of plasma are similar for the three configurations.

The connection length (L_c) is often used to evaluate the magnetic field structure. L_c is obtained by tracing the magnetic field lines and integrating the length using the KMAG code [23, 24]. Ideally, L_c should be infinite in the confinement region. Tracing of a magnetic field line is initiated at the starting position of a poloidal section. The calculation is terminated when the condition $L_c > 500$ m is satisfied. In the peripheral plasma region, L_c is finite, and the tracing calculation is terminated when a magnetic field line touches a vacuum wall surface. The tracing is performed in both the clockwise and counterclockwise toroidal directions. L_c is the sum of the path lengths from the starting point to the two termination points on the vacuum chamber surface in the two directions. Figure 3 shows the L_c distribution for a toroidal angle $\phi = 22.5°$ for the three configurations. The confinement region with $L_c > 500$ m is isolated from the chamber wall by the SOL region with $L_c < 200$ m. There are seven X-point like structures in the SOL. The middle of the two X-points is called an O-point region. There is a characteristic structure similar to the private flux region (PFR) in tokamaks, in the middle of two divertor legs connected to a given X-point. A pair of divertor legs is connected to the X-point between them and touch the chamber wall locally as discussed

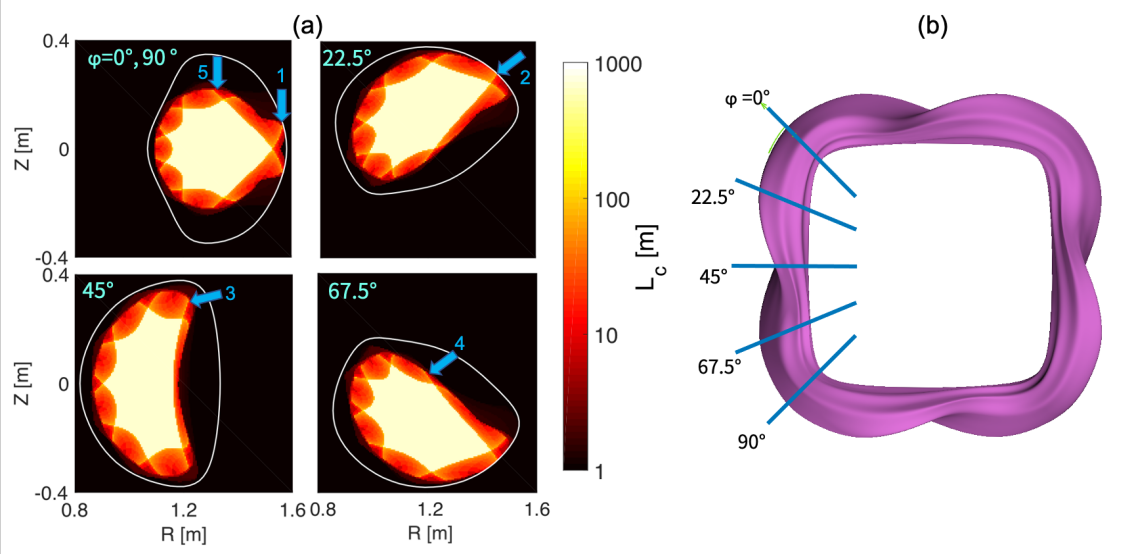

Figure 1. (a) Connection length distribution of the standard (medium bumpiness) configuration. (b) Top view of Heliotron J plasma. Each toroidal angle corresponds to an angle in (a).

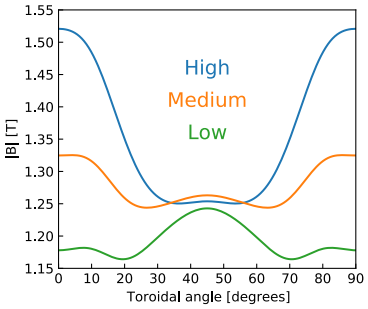

Figure 2. Magnetic field strength along the magnetic-axis for high-, medium- and low-bumpiness configurations.

later (see section 2.3).

In helical devices, including Heliotron J, each divertor leg also has a helical structure, which rotates in the poloidal direction when it is traced in the toroidal direction. When a pair of divertor legs is traced along the helical structure, as shown by arrows 1 to 5 in figure 1 (a), divertor leg 1 is connected to divertor legs 2-5 in different toroidal sections. These features of the SOL magnetic field structure are basically the same in the three configurations discussed in this paper.

2.2. Set up and physical parameters of transport code

The 3D peripheral plasma transport code EMC3-EIRENE [12] solves Braginskii's fluid equations along the magnetic field lines. The cross-field transport is modeled as a diffusion process under the assumption of anomalous transport. The 3D grids for

Heliotron J were developed with the aid of the grid generation tool FLARE [20, 25].

EMC3-EIRENE calculations were carried out for each magnetic configuration with conditions that were based on previous study[20]. The plasma heating power was assumed to be 320 kW. The input power was equally distributed to electrons and ions. Thus, electrons and ions both received 160 kW of power. The electron density at the upstream boundary (minor radius, $\rho \sim 0.8$) is set to be $n_{\mathrm{eu}} = 0.8 \times 10^{19}\ \mathrm{m}^{-3}$, a typical value for Heliotron J[26]. The perpendicular particle and heat transport coefficients were assumed to be $D = 1.0\ \mathrm{m}^2/\mathrm{s}$ and $\chi = 3.0\ \mathrm{m}^2/\mathrm{s}$ respectively. These transport coefficients were chosen to be consistent with the results of the Thomson scattering measurements[27]. Figure 4 shows the electron density n_{e} and temperature T_{e} for the three magnetic configurations on the poloidal cross section at $\phi = 22.5°$. The distributions of electron density and electron temperature are closely related to the magnetic field structure shown in figure 3. The electron density and temperature are very low in the region of $L_c < 10$ m. Thus, it is confirmed that the plasma region coincides with the region with a long connection length. An analysis of the connection length provides a plasma distribution independently of discharge conditions. However, it was found that the distributions of n_{e} and T_{e} around the divertor legs were different. The T_{e} distribution has clear structures corresponding to the divertor legs depicted by the connection length, and the poloidal distribution of n_{e} is broader than T_{e}. The difference in the n_{e} and T_{e} distributions is thought to be caused by the difference in the source location for particle and heat. In this calculation model, we assume that the heat source is ECH and is located at the core region of the plasma. On the other hand, the particle source is distributeed in the SOL region as the result of the recycling from the chamber wall. Thus, the n_{e} distribution at the divertor region becomes broader than the T_{e} distribution.

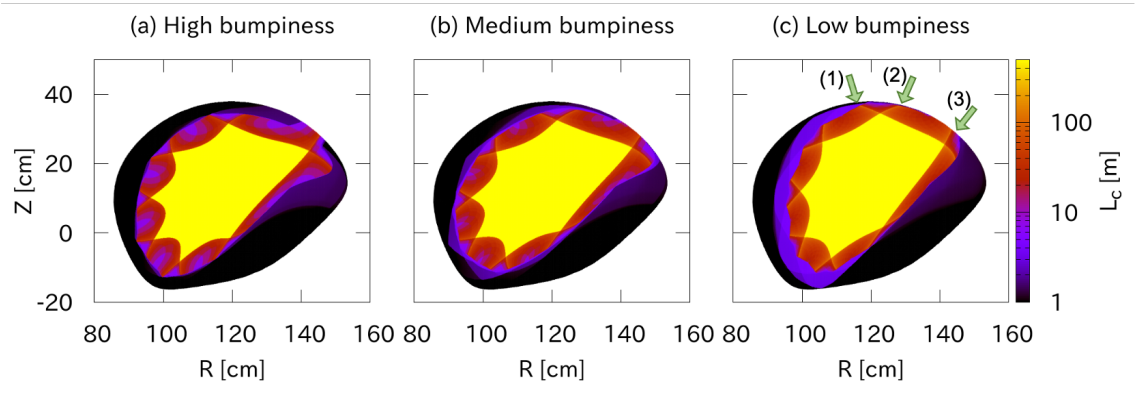

Figure 3. Connection length distribution for the (a) high-, (b) medium-, and (c) low-bumpiness configurations at $\phi = 22.5°$ poloidal cross section.

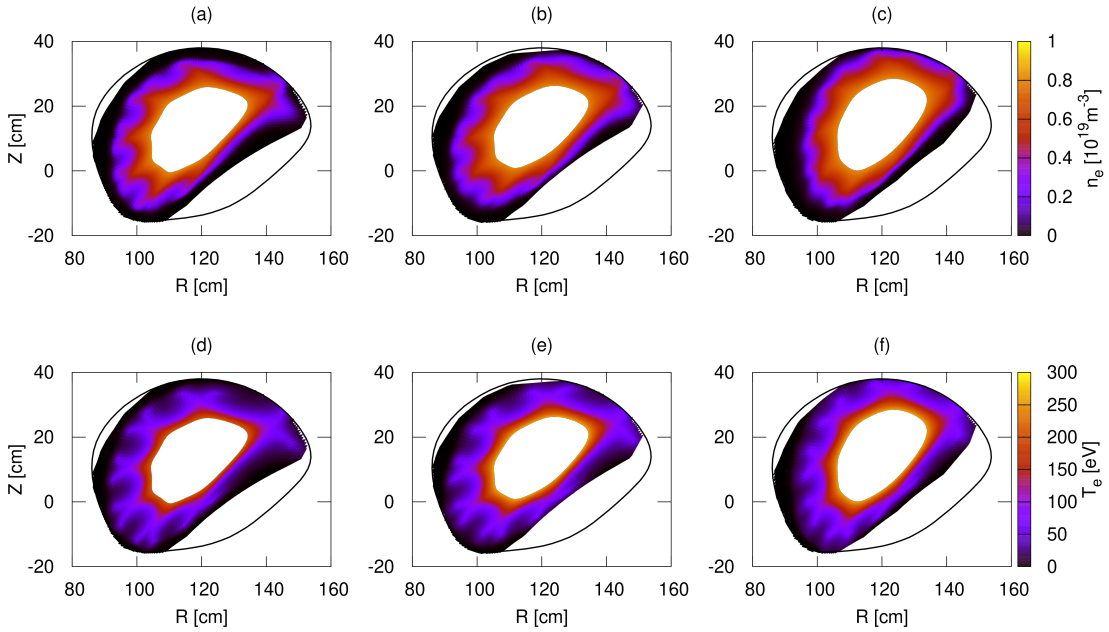

Figure 4. Electron density distribution for (a) high-, (b) medium-, and (c) low-bumpiness configurations at $\phi = 22.5°$ poloidal cross section. Electron temperature distribution for (d) high-, (d) medium-, and (f) low-bumpiness configurations.

2.3. Comparison of footprints of connection length and heat flux

A one-dimensional (1D) heat flux distribution on a particular poloidal cross section or an average toroidal distribution is insufficient for discussing the heat flux distribution because of the 3D structure of the divertor legs (see section 2.1). Figures 5 and 6 show the two-dimensional (2D) distributions of L_c and the heat flux footprint on the chamber wall for high-, medium-, and low-bumpiness configurations, respectively. Overall, the L_c distribution captures the heat flux distribution, as expected. The long magnetic field lines are connected to the peak position of the heat flux footprint. These lines are thought to be a major channel for heat transport to the surface. However, at some locations, there are peaks of heat flux deposition without a long connection length. For example, three locations with significant heat flux across $\phi = 22.5°$ were found in the low-bumpiness configuration, as shown by arrows 1 to 3 in figure 6 (c). These heat flux lines correspond to the positions of the divertor legs labeled 1 to 3 in figure 3 (c) respectively. Even if there is no footprint in the L_c distribution on the vacuum chamber surface, the divertor legs can exist with very small gap to the vacuum wall surface, and perpendicular heat flux contributes to the heat load at the location mentioned above. These results imply that although field line tracing is effective for estimating the heat flux distribution, some fine structures in the heat flux cannot be explained by the connection length, and thus 3D transport modeling is required to understand the physics of heat and particle transport in 3D toroidal devices. However, the model calculation is

based on some assumptions such as transport coefficients, and the result is affected by these assumptions. The modeling may not reproduce experimental result quantitatively if the assumptions are not valid. The advantage of the field line tracing is that it can predict heat load location roughly, without any assumptions, independently of specific discharge conditions. Both field line tracing and model calculations are important, and when used together, they can help qualitative understanding of transport processes in complicated 3D magnetic fields.

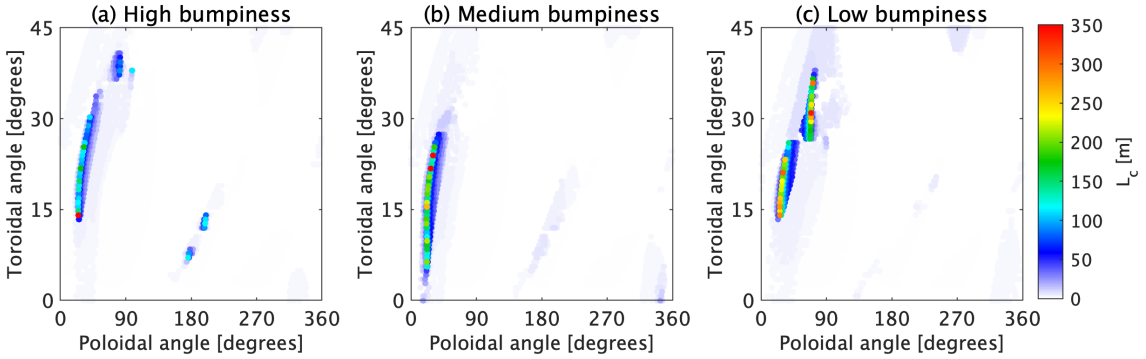

Figure 5. Connection length distribution for (a) high-, (b) medium-, and (c) low-bumpiness configurations on the whole chamber wall.

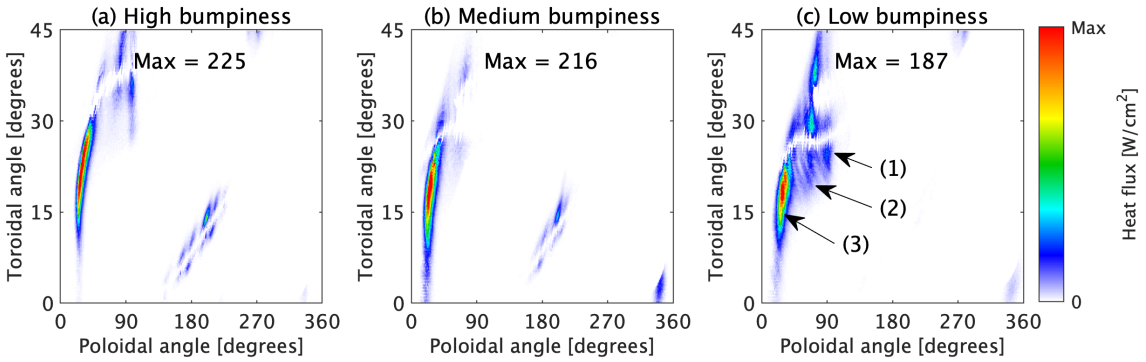

Figure 6. Heat flux distribution for (a) high-, (b) medium-, and (c) low-bumpiness configurations on the whole chamber wall.

3. Influence of magnetic configurations and electron density on heat load

The upstream electron density, n_{eu}, was scanned from 0.4×10^{19} to 3.0×10^{19} m^{-3} in each configuration to study the dependence of the heat flux on the plasma parameter in the confinement region. The input power and transport coefficients were fixed at the values given in section 2.

3.1. Dependence of peak heat load

The poloidal heat flux distributions at the toroidal position with the highest peak are shown in figure 7. The peak position for the heat flux is almost identical to the position with a long connection length. When the upstream electron density is increased, the maximum heat flux on the wall decreases significantly, and the heat flux profile broadens. The broadening of the heat load distribution at high density can be caused by several physical processes. The cross-field heat transport could decrease due to the moderate temperature gradient at high density. Also, the electron density distribution and parallel flow could be modified due to the change in ionization amount and distribution. Further analysis is needed to determine the dominant factor and to evaluate the effects quantitatively. A similar n_e dependence was observed for all three configurations, as shown in figures 7 (a)-(c). In addition, the heat flux on the O-point side is more significantly enhanced than that on the PFR side. It is likely that the SOL magnetic field structure induces this asymmetric variation of the heat flux; further analysis is necessary.

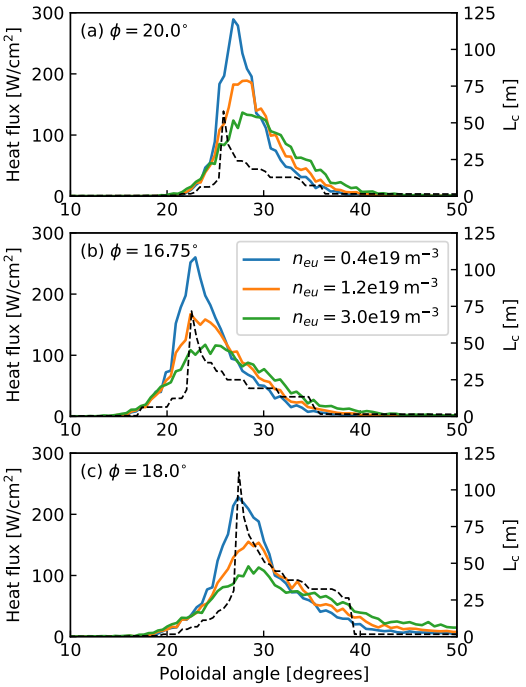

Figure 7. Solid lines indicate the heat flux distributions for (a) high-, (b) medium-, and (c) low-bumpiness configurations on the poloidal cross section for various electron densities. The black dashed line indicates the connection length distribution at a given position. The right- and left-hand sides of the L_c peak are the O-point side and PFR side, respectively.

3.2. Dependence of 2D heat load distribution

A detailed comparison of the 2D heat flux distribution is shown in figure 8. The figure is an enlarged view of the 2D heat flux distributions at the lowest electron density ($n_{eu} = 0.4 \times 10^{19}$ m^{-3}) and the highest electron density ($n_{eu} = 3.0 \times 10^{19}$ m^{-3}) for the high-, medium-, and low-bumpiness configurations. The peak value of the heat flux at high electron density is much lower than that at low electron density case. This is consistent with the dependence shown in figure 7. In addition, the position of the heat flux footprint shifts in the toroidal/poloidal direction when n_{eu} is increased. The black dotted lines in figure 8 indicate the peak poloidal positions of L_{c} for each configuration. The right and left sides of the divertor leg are the O-point side and the PFR side, respectively. At low electron density, the poloidal peak position of the heat flux is close to the peak of L_{c}, whereas at high electron density, it shifts to the SOL side of the divertor leg. The change of the peak position may have been caused by the difference in transport properties between the two sides of the divertor leg, which is related to the difference in the magnetic field structure.

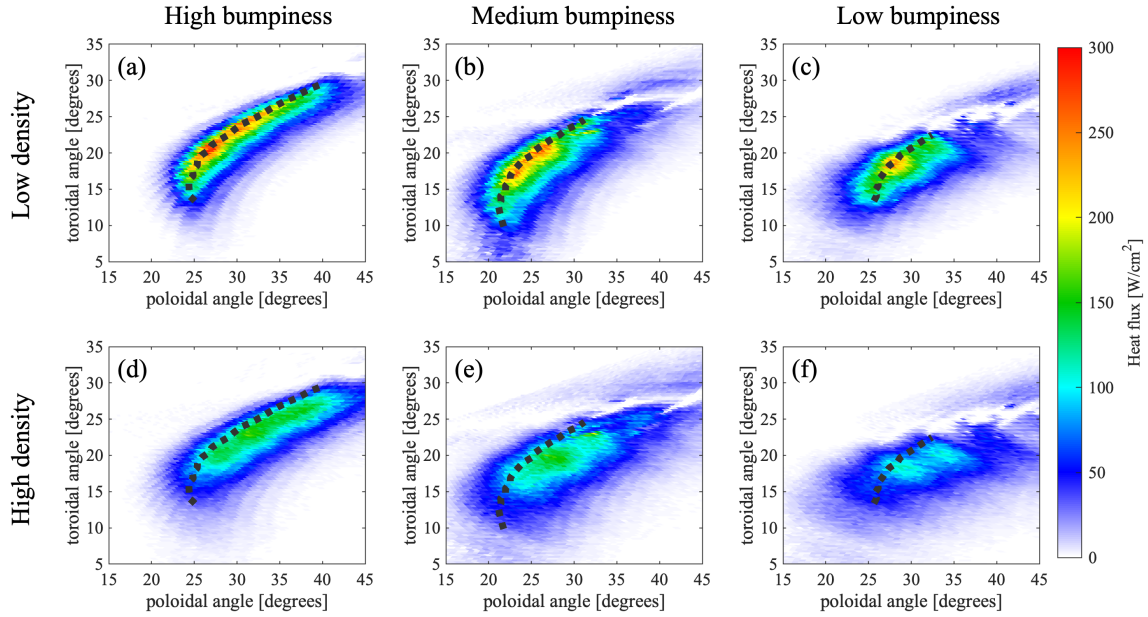

Figure 8. 2D heat flux distributions for (a) high-, (b) medium-, and (c) low-bumpiness configurations at low electron density. (d), (e), and (f) show the results obtained at high electron density, respectively. The black dotted line shows the peak position of L_{c}. The position is the same in each configuration. The right side of the divertor leg is the O-point side.

3.3. Dependence of heat load dispersion on chamber wall

The local peak value of the heat flux and its position are affected by geometric and local factors such as the angle of the magnetic field and the vacuum chamber. The

distribution around the peak position also depends on the shape of the chamber wall. To describe the global properties of the heat flux distribution on all plasma-facing surfaces and to compare distributions, a statistical distribution function related to the footprint is preferable. The histogram of the L_c for Heliotron J was employed in [28], and the arithmetic mean of L_c was obtained. Similarly, a heat distribution function for the whole chamber wall is introduced in this study. The dependence of the heat flux distribution on the upstream electron density and the magnetic configurations is investigated to obtain the characteristics of the global distribution of the heat load on the chamber wall. The distribution function is obtained using the following procedure.

The chamber wall is defined as a large number of rectangular cells with finite width in the poloidal and toroidal directions. The value of the heat flux on each cell is evaluated. We consider N cells covering the whole chamber wall. The cells are labeled as i ($i = 1, 2, 3, ..., N$). The heat flux on a cell and the area of the cell are denoted by f_i [W/m^2] and s_i [m^2] respectively. The power deposited on the cell h_i [W] is given as follows.

$$h_i = f_i s_i \tag{1}$$

We consider a group of cell indexes A where the heat flux is in the following range:

$$A(f) = \{i \,|f < f_i < f + \Delta f\}. \tag{2}$$

The total power for cells belonging to $A(i\Delta f)$ is

$$F_A(i\Delta f) = \sum_{j \in A(i\Delta f)} f_j s_j. \tag{3}$$

Finally, the discretized heat flux distribution function is defined as follows:

$$H_i = \frac{1}{\Delta f} F_A(i\Delta f). \tag{4}$$

The value of H_i indicates the total power [W] given by the heat flux with $i\Delta f < f < (i+1)\Delta f$. The integral of H_i is the total power deposited on the whole chamber wall. We note that the total power deposited does not significantly depend on the magnetic configuration or $n_{\rm eu}$ value, because the input power is fixed and radiation loss due to impurities is not considered in this study. In this analysis, Δf is set to 0.1 MW/m^2.

The configuration dependence of H_i is shown in figure 9 (a). In the low-bumpiness configuration, the maximum heat flux is more than 15% lower than that for the high-bumpiness case, and the heat flux in the low-heat-flux region (< 0.5 MW/m^2) is higher than that in the other two configurations. The $n_{\rm eu}$ dependence of H_i for the medium-bumpiness configuration is shown in figure 9 (b). The maximum heat flux decreases and the power carried by low heat flux increases when $n_{\rm eu}$ is high. A similar $n_{\rm eu}$ dependence was also observed for the high- and low-bumpiness configurations. The dependence of $n_{\rm eu}$ and the magnetic configuration is consistent with the discussion in section 3.2. The decrease of the high heat flux and the increase of the low heat flux suggest the dispersion of the heat load on the chamber wall. The peak of H_i is in the low heat flux region (less

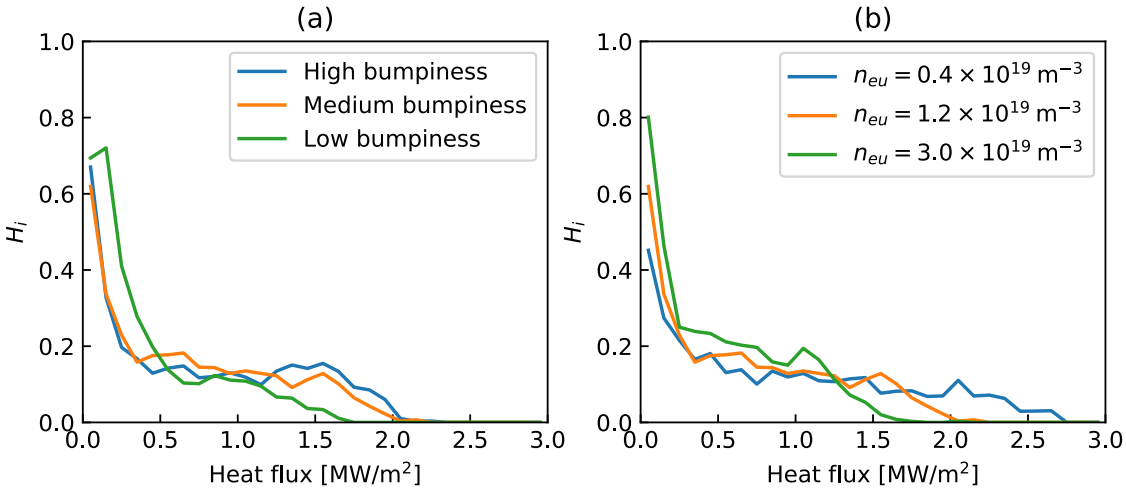

Figure 9. Power distribution results. (a) Configuration dependence under a fixed upstream electron density; $n_{eu} = 1.2 \times 10^{19}$ m^{-3}. (b) $n_{\rm eu}$ dependence for medium-bumpiness configuration.

than 0.2 MW/m^2) for all calculation conditions. These results suggest that the highest heat flux provides only part of the power to the plasma-facing wall and that the low heat flux provides a non-negligible amount of power deposition. However, a quantitative evaluation of the peak value in the very-low-heat-flux region and the distribution around the peak is difficult to perform using the current model because of the low resolution of the grid, and because the chamber surface possibly affects the heat flux distribution sensitively.

4. Summary

The distributions of the connection length and heat flux on the chamber wall of Heliotron J were calculated with EMC3-EIRENE for three magnetic configurations (high, medium, and low bumpiness), and the dependence on the upstream electron density was discussed. The footprints of the connection length calculated with the field line tracing code and the heat load distribution obtained with transport modeling were compared. Field line tracing was effective for estimating the divertor heat load distributions because the divertor leg with long $L_{\rm c}$ is the main channel of heat transport to the chamber wall. However, some additional footprints of the heat flux were observed with transport modeling. 3D transport modeling is required to capture the fine structures of heat flux.

The 1D heat flux distribution in the poloidal cross section and the 2D heat flux distribution in the toroidal and poloidal directions on the chamber wall were modeled under various $n_{\rm eu}$ conditions. Expansion and displacement of the heat flux distribution were observed at higher $n_{\rm eu}$ conditions. The $n_{\rm eu}$ dependence is different on the O-point and PFR sides (i.e., the two sides of the divertor leg in the poloidal direction). This asymmetry is likely induced by the difference in the magnetic field structure between

the O-point side and the PFR side.

A heat distribution function was introduced to obtain statistical information on the power distribution on the whole chamber wall independently of geometric and local factors. A decrease of the high-heat-flux region and an increase of the low-heat-flux region were observed at higher n_{eu} conditions. The total heat deposited on the chamber wall did not decrease because of the fixed input power and lack of radiation loss due to impurities. Thus, the reduction in the maximum heat flux was caused by the dispersion of power. A dispersion of the heat load was also observed by changing the magnetic configuration. For the low-bumpiness configuration, the peak heat flux was more than 15% lower than that for the high-bumpiness configuration. These results demonstrate that the configuration is an optimization parameter for the reduction of the divertor heat load in 3D toroidal devices. Modeling studies that include impurity radiation and experimental verifications are needed for a quantitative evaluation of the heat flux distribution. An analysis that uses a heat distribution function can be applied to a multi-machine comparison of the heat flux dispersion by normalizing the input power and the surface area.

Acknowledgments

The authors are grateful to the Heliotron J staff for useful discussion. This work was supported in part by JSPS KAKENHI Grant Numbers 16K18340 and 19K03802. This work was performed with the support and under the auspices of the NIFS Collaborative Research Program (NIFS10KUHL030, NIFS17KUHL081) and "PLADyS", JSPS Core-to-Core Program, A. Advanced Research Networks.

[1] Eich T, Sieglin B, Scarabosio A, Fundamenski W, Goldston R J and Herrmann A 2011 *Phys. Rev. Lett.* **107** 215001

[2] Eich T, Leonard A W, Pitts R A, Fundamenski W, Goldston R J, Gray T K, Herrmann A, Kirk A, Kallenbach A, Kardaun O, Kukushkin A S, Labombard B, Maingi R, Makowski M A, Scarabosio A, Sieglin B, Terry J and Thornton A 2013 *Nucl. Fusion* **53** 093031

[3] Asakura N, Shimizu K, Hoshino K, Tobita K, Tokunaga S and Takizuka T 2013 *Nucl. Fusion* **53** 123013

[4] Asakura N, Hoshino K, Suzuki S, Tokunaga S, Someya Y, Utoh H, Kudo H, Sakamoto Y, Hiwatari R, Tobita K, Shimizu K, Ezato K, Seki Y, Ohno N and Ueda Y 2017 *Nucl. Fusion* **57** 126050

[5] Ryutov D D, Cohen R H, Rognlien T D and Umansky M V 2012 *Plasma Phys. Control. Fusion* **54** 124050

[6] Ryutov D D and Soukhanovskii V A 2015 *Phys. Plasmas* **22** 110901

[7] Evans T E, Moyer R A, Burrell K H, Fenstermacher M A X E, Joseph I, Leonard A W, Osborne T H, Porter G D, Schaffer M J, Snyder P B, Thomas P R, Watkins J G and West W P 2006 *Nat. Phys.* **2** 419–423

[8] Evans T E, Moyer R A and Watkins J G 2008 *Nucl. Fusion* **48** 024002

[9] Frerichs H, Reiter D, Schmitz O, Cahyna P, Evans T E, Feng Y and Nardon E 2012 *Phys. Plasmas* **19** 052507

[10] Brida D, Lunt T, Wischmeier M, Bernert M, Carralero D, Faitsch M, Feng Y, Sehmer T, Sieglin B, Suttrop W and Wolfrum E 2017 *Nucl. Fusion* **57** 116006

[11] Kobayashi M, Xu Y, Ida K, Corre Y, Feng Y, Schmitz O, Frerichs H, Tabares F L, Evans T E, Coenen J W, Liang Y, Bader A, Itoh K, Yamada H, Ghendrih P, Ciraolo G, Tafalla D, Lopez-Fraguas A, Guo H Y, Cui Z Y, Reiter D, Asakura N, Wenzel U, Morita S, Ohno N, Peterson B J and Masuzaki S 2015 *Nucl. Fusion* **55** 104021

[12] Feng Y, Sardei F, Kisslinger J, Grigull P, Mccormick K and Reiter D 2004 *Contrib. Plasma Phys.* **44** 57–69

[13] Reiter D, Baelmans M and Börner P 2005 *Fusion Sci. Technol.* **47** 172–186

[14] Effenberg F, Pedersen T S, Hölbe H, Krychowiak M, Feng Y, König R, Reiter D, Schmitz O, Frerichs H, Stephey L and Bozhenkov S 2017 *Nucl. Fusion* **57** 036021

[15] Akerson A R, Bader A, Hegna C C, Schmitz O, Stephey L A, Anderson D T, Anderson F S and Likin K M 2016 *Plasma Phys. Control. Fusion* **58** 084002

[16] Kawamura G, Tanaka H, Mukai K, Peterson B, Dai S Y, Masuzaki S, Kobayashi M, Suzuki Y, Feng Y and Group L E 2018 *Plasma Phys. Control. Fusion* **60** 084005

[17] Lunt T, Feng Y, Bernert M, Herrmann A, De Marné P, McDermott R, Müller H W, Potzel S, Pütterich T, Rathgeber S, Suttrop W, Viezzer E, Wolfrum E and Willensdorfer M 2012 *Nucl. Fusion* **52** 054013

[18] Huang J, Feng Y, Wan B, Liu S, Chang J, Wang H, Gao W, Zhang L, Gao W, Chen Y, Wu Z and Wu C 2014 *Plasma Phys. Control. Fusion* **56** 075023

[19] Obiki T, Mizuuchi T, Nagasaki K, Okada H, Sano F, Hanatani K, Liu Y, Hamada T, Manabe Y, Shidara H, Ang W L, Ikeda Y, Kobayashi T, Takamiya T, Takeda M, Ijiri Y, Senju T, Yaguchi K, Sakamoto K, Toshi K, Shibano M, Kondo K, Besshou S, Nakamura Y, Nakasuga M, Wakatani M, Yamagishi O, Aizawa K, Kawazome Y, Maeno S and Tomiyama K 2001 *Nucl. Fusion* **41** 833–844

[20] Matoike R, Kawamura G, Ohshima S, Kobayashi M, Suzuki Y, Nagasaki K, Masuzaki S, Kobayashi S, Yamamoto S, Kado S, Minami T, Okada H, Konoshima S, Mizuuchi T, Tanaka H, Matsuura H, Feng Y and Frerichs H 2019 *Plasma Fusion Res.* **14** 3403127

[21] Mizuuchi T, Sano F, Nagasaki K, Okada H, Kobayashi S, Hanatani K, Torii Y, Ijiri Y, Senju T, Yaguchi K, Sakamoto K, Toshi K, Shibano M, Kondo K, Nakamura Y, Kaneko M, Arimoto H, Motojima G, Fujikawa S, Kitagawa H, Nakamura H, Tsuji T, Uno M, Watanabe S, Yabutani H, Matsuoka S, Nosaku M, Watanabe N, Yamamoto S, Watanabe K Y, Suzuki Y and Yokoyama M 2006 *Fusion Sci. Technol.* **50** 352–360

[22] Yokoyama M and Watanabe K Y 2005 *Nucl. Fusion* **45** 1600–1607

[23] Wakatani M, Nakamura Y, Kondo K and Nakasuga M 2000 *Nucl. Fusion* **40** 569

[24] Nakamura Y 1993 *Plasma Fusion Res.* **69** 41

[25] Frerichs H, Reiter D, Feng Y and Harting D 2010 *Comput. Phys. Commun.* **181** 61–70

[26] Sano F, Mizuuchi T, Kondo K, Nagasaki K, Okada H, Kobayashi S, Hanatani K, Nakamura Y, Yamamoto S, Torii Y, Suzuki Y, Shidara H, Kaneko M, Arimoto H, Azuma T, Arakawa J, Ohashi K, Kikutake M, Shimazaki N, Hamagami T, Motojima G, Yamazaki H, Yamada M, Kitagawa H, Tsuji T, Nakamura H, Watanabe S, Murakami S, Nishino N, Yokoyama M, Ijiri Y, Senju T, Yaguchi K, Sakamoto K, Tohshi K and Shibano M 2005 *Nucl. Fusion* **45** 1557–1570

[27] Kenmochi N, Minami T, Takahashi C, Mochizuki S, Nishioka K, Kobayashi S, Nagasaki K, Nakamura Y, Okada H, Kado S, Yamamoto S, Ohshima S, Konoshima S, Weir G M, Otani Y and Mizuuchi T 2017 *Plasma Phys. Control. Fusion* **59**

[28] Mizuuchi T, Nakasuga M, Sano F, Nakamura Y, Nagasaki K, Okada H, Kondo K and Obiki T 2001 *J. Nucl. Mater.* **290-293** 678–682